Acta Crystallographica Section A
**Foundations of Crystallography**
ISSN 0108-7673

Received 30 July 2009
Accepted 5 July 2010



# Integral modeling approach to study the phase behavior of complex solids: application to phase transitions in $MgSiO_3$ pyroxenes

**Sandro Jahn**

Deutsches GeoForschungsZentrum GFZ, Telegrafenberg, 14471 Potsdam, Germany.
Correspondence e-mail: jahn@gfz-potsdam.de

A combination of electronic structure calculations, classical molecular dynamics simulations and metadynamics is proposed to study the phase behavior of complex crystals. While the former provide accurate energetics for thermodynamic properties, molecular dynamics and metadynamics simulations may reveal new metastable phases and provide insight into mechanisms and kinetics of the respective structural transformations. Here, different simulation methods are used to investigate the polymorphism of $MgSiO_3$ pyroxenes (enstatites) up to high pressures and temperatures. A number of displacive phase transitions are observed within the three basic structure types clino-, ortho- and protoenstatite using classical molecular dynamics simulations. Transitions between these types require a change of stacking order, which is modeled using a combination of molecular dynamics and metadynamics.

## 1. Introduction

The understanding of the phase behavior of complex materials has many practical aspects. It is of primary importance to identify the thermodynamically stable phase assembly at a given pressure, $P$, temperature, $T$, and chemical composition, $x$, which is characterized by the global minimum of the Gibbs free energy, $G$. However, kinetic effects often prevent the formation of the most stable (bulk) phases. This may be desired, for example, in the fast expanding area of materials design but sometimes can also have severe consequences. For instance, metastable olivine ($\alpha$-$Mg_2SiO_4$) is thought to be involved in the generation of deep earthquakes (Green, 2007).

Computer simulations are becoming increasingly powerful in the structure prediction of materials and determination of phase diagrams (Schön & Jansen, 1996; Martoňák *et al.*, 2003; Oganov & Glass, 2006). This is due to the vast increase in computing power and also to new efficient algorithms. One of the key questions that remains is how to represent particle interactions accurately at reasonable computational cost. For complex materials with hundreds of atoms in the unit cell, accurate electronic structure calculations, for example within density-functional theory (DFT), may be prohibitively expensive, especially regarding dynamic properties. Classical potentials, on the other hand, may not represent the total energy of a system accurately enough to provide a quantitative picture of the phase behavior. Hence, there is continuous need for further methodological developments in materials modeling.

The studies presented here make use of a combination of accurate DFT calculations to calculate lattice free energies (or enthalpies at zero temperature) and classical interaction potentials to explore phase changes in pyroxenes that constitute a complex class of geomaterials. Pyroxenes are important rock-forming minerals with the general formula $M1M2T_2O_6$. The structures consist of a more or less close-packed oxygen (O) sublattice with cations in tetrahedral ($T$) and two different octahedral sites ($M1$ and $M2$). In the following, we concentrate on the enstatite composition $MgMgSi_2O_6$ or, in short, $MgSiO_3$, *i.e.* the $T$ sites are occupied by Si and the $M$ sites by Mg. As shown in Fig. 1, the $SiO_4$ tetrahedra are corner-linked and form infinite chains. One distinction between different pyroxene structures is the stacking of these chains that are linked together *via* $MgO_6$ octahedra. In clinopyroxenes all octahedra have the same orientation, whereas an alternating sense of orientation is observed in protopyroxenes. In orthopyroxenes, the octahedral orientation is changed after two layers with the same orientation (see Fig. 1). The second distinctive feature between different pyroxene polymorphs is the relative rotation of $SiO_4$ tetrahedra within the chain. For large octahedral cations or towards high temperatures the chains are expected to be elongated, whereas for small cations or at high pressure the chains are more tilted. This is explained by the relatively small compressibility of the $SiO_4$ tetrahedra. Depending on the sense of rotation, either O- or S-rotated chains may be formed (see Fig. 2).

The phase diagram of $MgSiO_3$ is reasonably well understood (Presnall, 1995) and contains stability fields for five

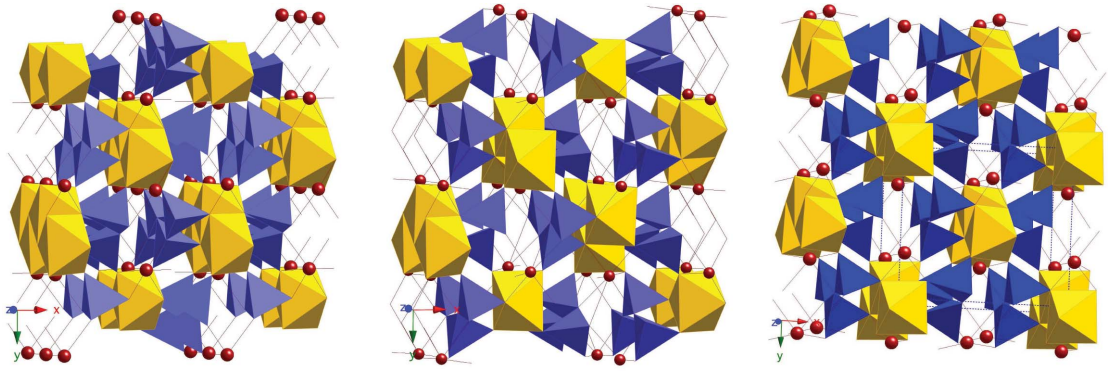


**Figure 1**
Three structure types of pyroxenes characterized by different stacking of the $SiO_4$ tetrahedral chains: (*a*) clinopyroxene, (*b*) orthopyroxene and (*c*) protopyroxene. This leads to different orientations of the $MgO_6$ octahedra. Mg on *M*2 sites are represented by balls.

different enstatite polymorphs. The ground-state structure at ambient conditions is assumed to be low-clinoenstatite (space group $P2_1/c$). With increasing temperature, low-clinoenstatite transforms into orthoenstatite (*Pbca*) at about 850 K, further into protoenstatite (*Pbcn*) at about 1300 K, and into another high-*T* clinoenstatite with space group $C2/c$ just below the melting point at about 1850 K. Towards high pressures, protoenstatite and high-*T* clinoenstatite transform into orthoenstatite below 1 GPa. At higher pressures (above 7 to 12 GPa), both orthoenstatite and low-clinoenstatite transform into high-*P* clinoenstatite ($C2/c$). From topological studies of ideal pyroxene structures (Thompson & Downs, 2003) additional phases are suggested, some of which may exist as metastable phases in the enstatite system. Indeed, there is experimental evidence for high-pressure phases related to orthoenstatite (Lin, 2003; Kung *et al.*, 2004) and protoenstatite (Yang *et al.*, 1999). Recent molecular dynamics simulations and DFT calculations confirm these predictions, which will be discussed in detail below. The second goal of this paper is to discuss mechanisms of phase transitions within the different structure types (clino-, ortho- and protoenstatite) and also between them.

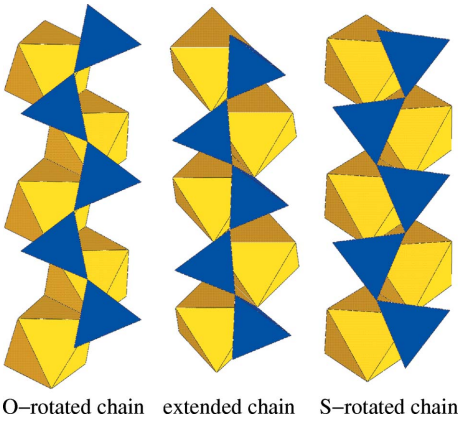


**Figure 2**
Different types of rotation within the $SiO_4$ chain to accommodate size mismatch between octahedral and tetrahedral layers. Extended chains are observed for the largest octahedra. Smaller octahedra cause a tilt of the tetrahedra. For S rotations, the basal triangle of the tetrahedron rotates towards the same orientation as the parallel triangle of the octahedra; for O rotations the tilt is in the opposite direction.

## 2. Computational methods

For this study, three different computational methods are used. Electronic structure calculations within DFT are performed using the plane-wave code *ABINIT* (Gonze *et al.*, 2002, 2005). The exchange correlation functional is treated within the local density approximation (LDA) (Perdew & Zunger, 1981). A plane-wave energy cutoff of 1000 eV is used in combination with optimized norm-conserving pseudopotentials (Rappe *et al.*, 1990). The Brillouin-zone sampling is performed with a suitable Monkhorst–Pack grid (Monkhorst & Pack, 1976). All DFT calculations are performed at zero temperature. Full cell optimizations are performed to obtain the enthalpy curves at different pressures.

The finite temperature behavior is explored using classical molecular dynamics simulations. The particle interactions are described by an advanced ionic interaction model (AIM) (Aguado *et al.*, 2003; Madden *et al.*, 2006) which is optimized by reference to electronic structure calculations and shows a high degree of accuracy and transferability for silicates (Jahn & Madden, 2007). The AIM potential $V$ is constructed from four components,

$$V = V^{qq} + V^{\text{energy-dispersive}} + V^{\text{rep}} + V^{\text{pol}}. \quad (1)$$

The first two components, the Coulomb interaction between point charges ($V^{qq}$) and van der Waals dispersion interactions ($V^{\text{energy-dispersive}}$), are pairwise additive,

$$V^{qq} = \sum_{i<j} \left(q^i q^j / r_{ij}\right), \quad (2)$$

$$V^{\text{energy-dispersive}} = -\sum_{i<j} \left\{\left[1 - g_6^{ij}(r_{ij})\right] C_6^{ij}/r_{ij}^6 + \left[1 - g_8^{ij}(r_{ij})\right] C_8^{ij}/r_{ij}^8\right\}. \quad (3)$$

$q^i$ is the formal charge on ion $i$ (+4 for Si, +2 for Mg and −2 for O), and $C_6^{ij}$ and $C_8^{ij}$ are the dipole–dipole and dipole–quadrupole dispersion coefficients, respectively. $g_6^{ij}(r_{ij})$ and $g_8^{ij}(r_{ij})$

are Tang–Toennies dispersion damping functions of the form (Tang & Toennies, 1984)

$$g_n^{ij}(r_{ij}) = c_n^{ij}\exp\left(-b_n^{ij}r_{ij}\right)\sum_{k=0}^{k_{\max}}\left[\left(b_n^{ij}r_{ij}\right)^k/k!\right], \quad (4)$$

which describe short-range corrections to the asymptotic dispersion term. We set $k_{\max} = 6$, $c_6^{ij} = c_8^{ij} = 1$ and $b_6^{ij} = b_8^{ij} = b^{ij}_{\text{energy-dispersive}}$ (see Table 1).

The overlap repulsion component ($V^{\text{rep}}$) is given by

$$\begin{aligned} V^{\text{rep}} = &\sum_{i\in\text{O},\, j\in\text{Mg,Si}}\left[A^{ij}\exp(-a^{ij}\rho^{ij}) + B^{ij}\exp(-b^{ij}\rho^{ij})\right. \\ &\left. + C^{ij}\exp\left(-c^{ij}r_{ij}\right)\right] + \sum_{i,\,j\in\text{O}} A^{ij}\exp\left(-a^{ij}r_{ij}\right) \\ &+ \sum_{i\in\text{O}}\left\{D\left[\exp(\beta\delta\sigma^i) + \exp(-\beta\delta\sigma^i)\right]\right. \\ &\left. + \left[\exp\left(\zeta^2|\nu^i|^2\right) - 1\right] + \left[\exp\left(\eta^2|\kappa^i|^2\right) - 1\right]\right\} \quad (5) \end{aligned}$$

with

$$\rho^{ij} = r_{ij} - \delta\sigma^i - S_\alpha^{(1)}\nu_\alpha^i - S_{\alpha\beta}^{(2)}\kappa_{\alpha\beta}^i \quad (6)$$

and summation of repeated indexes is implied. The variable $\delta\sigma^i$ characterizes the deviation of the radius of oxide anion $i$ from its default value, $\{\nu_\alpha^i\}$ are a set of three variables describing the Cartesian components of a dipolar distortion of the ion, and $\{\kappa_{\alpha\beta}^i\}$ are a set of five independent variables describing the corresponding quadrupolar shape distortions $[|\kappa|^2 = \kappa_{xx}^2 + \kappa_{yy}^2 + \kappa_{zz}^2 + 2(\kappa_{xy}^2 + \kappa_{xz}^2 + \kappa_{yz}^2)$ with a traceless matrix $\kappa]$. $S_\alpha^{(1)} = r_{ij,\alpha}/r_{ij}$ and $S_{\alpha\beta}^{(2)} = 3r_{ij,\alpha}r_{ij,\beta}/r_{ij}^2 - \delta_{\alpha\beta}$ are interaction tensors. The last summations include the self-energy terms, representing the energy required to deform the anion charge density, with $\beta$, $\zeta$ and $\eta$ as effective force constants. The extent of each ion's distortion is determined at each molecular dynamics time step by energy minimization.

The polarization part of the potential incorporates dipolar and quadrupolar contributions (Wilson *et al.*, 1996),

$$\begin{aligned} V^{\text{pol}} = &\sum_{i,\,j\in\text{O}}\left[(q^i\mu_\alpha^j - q^j\mu_\alpha^i)T_\alpha^{(1)}\right. \\ &+ \left(q^i\theta_{\alpha\beta}^j/3 + \theta_{\alpha\beta}^i q^j/3 - \mu_\alpha^i\mu_\beta^j\right)T_{\alpha\beta}^{(2)} \\ &+ \left(\mu_\alpha^i\theta_{\beta\gamma}^j/3 + \theta_{\alpha\beta}^i\mu_\gamma^j/3\right)T_{\alpha\beta\gamma}^{(3)} + \left(\theta_{\alpha\beta}^i\theta_{\gamma\delta}^j/9\right)T_{\alpha\beta\gamma\delta}^{(4)}\Big] \\ &+ \sum_{i\in\text{O},\, j\in\text{Mg,Si}}\left\{q^j\mu_\alpha^i\left[1 - g_D^{ij}(r_{ij})\right]T_\alpha^{(1)}\right. \\ &\left. + \left(\theta_{\alpha\beta}^i q^j/3\right)\left[1 - g_Q^{ij}(r_{ij})\right]T_{\alpha\beta}^{(2)}\right\} \\ &+ \sum_{i\in\text{O}}\left[(1/2\alpha)|\boldsymbol{\mu}^i|^2 + (1/6C)\theta_{\alpha\beta}^i\theta_{\alpha\beta}^i\right], \quad (7) \end{aligned}$$

where $\alpha$ and $C$ are the dipole and quadrupole polarizabilities of the oxygen ion, respectively, and $T_{\alpha\beta\gamma\delta} = \nabla_\alpha\nabla_\beta\nabla_\gamma\nabla_\delta\ldots(1/r_{ij})$ are the multipole interaction tensors (Stone, 1996). The instantaneous values of these moments are obtained by minimization of this expression. The charge-dipole and charge-quadrupole cation–anion asymptotic functions include terms which account for penetration effects at short range by using again Tang–Toennies damping functions [see equation (4)] with $n = D$ and $Q$ standing for the dipolar and quadrupolar parts, respectively. While the parameters $b_D^{ij}$ and $b_Q^{ij}$ determine the range at which the overlap of the charge densities affects the induced multipoles, the parameters $c_D^{ij}$ and $c_Q^{ij}$ determine the strength of the ion response to this effect. Only oxygen ions are considered polarizable. Details of the optimization of the AIM potential and transferability tests are given elsewhere (Jahn & Madden, 2007). The potential parameters relevant for this study are summarized in Table 1.

**Table 1**
AIM potential parameters in atomic units (from Jahn & Madden, 2007).

| Parameter | O—O | Mg—O | Si—O |
|---|---|---|---|
| $A^{ij}$ | 1068.0 | 41.439 | 43.277 |
| $a^{ij}$ | 2.6658 | 1.6588 | 1.5418 |
| $B^{ij}$ | | 59375 | 43962 |
| $b^{ij}$ | | 3.9114 | 3.9812 |
| $C^{ij}$ | | 6283.5 | 6283.5 |
| $c^{ij}$ | | 4.2435 | 4.2435 |
| $b_D^{ij}$ | | 2.2148 | 2.1250 |
| $c_D^{ij}$ | | 2.8280 | 1.5933 |
| $b_Q^{ij}$ | | 1.9300 | 1.9566 |
| $c_Q^{ij}$ | | 1.3317 | 1.0592 |
| $C_6^{ij}$ | 44.372 | 2.1793 | 2.1793 |
| $C_8^{ij}$ | 853.29 | 25.305 | 25.305 |
| $b^{ij}_{\text{energy-dispersive}}$ | 1.4385 | 2.2057 | 2.2057 |
| $D$ | 0.49566 | $\beta$ | 1.2325 |
| $\zeta$ | 0.89219 | $\eta$ | 4.3646 |
| $\alpha$ | 8.7671 | $C$ | 11.5124 |

Molecular dynamics (MD) simulations are performed at constant $P$ and $T$ using a simulation box with 640 ions (128 formula units of $MgSiO_3$). At each MD step, the energy of the 'electronic degrees of freedom' (ionic polarization and deformation) is minimized before the ions are moved. This effectively describes many-body interactions [for more details see Aguado *et al.* (2003)]. For the numerical integration of the equations of motion the Leapfrog algorithm (Allen & Tildesley, 1987) is used with a time step of 1 fs. Pressure and temperature are controlled using a barostat (Martyna *et al.*, 1994) coupled to a Nosé–Hoover thermostat (Nosé & Klein, 1983).

Finally, a combination of metadynamics and classical MD is used to study transitions that involve changes in the stacking sequence of the $SiO_4$ chains. The metadynamics algorithm is described by Martoňák *et al.* (2005, 2006). As collective variables the scaled box matrix is used. Between the metadynamics steps, short (1 ps) MD runs at constant volume and temperature are performed to relax the atomic positions and to obtain the pressure tensor. As metadynamics parameters, a Gaussian height of 8.32 eV and a Gaussian width of 2.88 $eV^{1/2}$ are used (Jahn & Martoňák, 2008, 2009).

## 3. Results from simulation studies

### 3.1. Displacive phase transitions

Displacive phase transitions between pyroxenes occur within the different structure types (Fig. 1) by rotation of the tetrahedra within the $SiO_4$ chains (Fig. 2). The stacking

sequence of the chains remains unchanged. These transitions are driven by temperature or pressure and usually require *in situ* experiments since the high-$T$ or high-$P$ structures easily revert under cooling or decompression, respectively. The most prominent displacive phase transitions in pyroxenes are transitions between different clinopyroxene phases. They have been subject to numerous experimental (Perrotta & Stephenson, 1965; Smith, 1969; Angel *et al.*, 1992) and computational (Mendelssohn & Price, 1997; Shimobayashi *et al.*, 2001; Miyake *et al.*, 2002) studies for $MgSiO_3$. Transitions are observed between low- ($P2_1/c$), high-$T$ ($C2/c$) and high-$P$ ($C2/c$) clinoenstatite. We are able to reproduce the transition from low- to high-$P$ clinoenstatite with the AIM in classical MD simulations (Jahn & Madden, 2007). At room temperature the transition occurs at about 10 GPa in compression and is reversed under decompression at about 1 GPa. The corresponding changes in the lattice parameters $a$, $b$ and $c$ are shown in Fig. 3. The observed range of transition pressures is consistent with experiment, where the bracket of the transition is between 5.3 and 8 GPa (Angel *et al.*, 1992). Inspection of the different structures reveals that in low-clinoenstatite half of the chains are O-rotated and half are S-rotated. High-$P$ clinoenstatite only consists of O-rotated chains, whereas in high-$T$ clinoenstatite the chains are essentially extended.

Similar transitions are also observed or predicted for the other structure types, orthoenstatite and protoenstatite. In the orthoenstatite system a high-temperature phase with *Cmca* symmetry was anticipated from Brillouin-scattering results (Jackson *et al.*, 2004) but MD simulations found an isosymmetric phase transition to a high-$T$ *Pbca* structure. The latter structure was recently confirmed by experiment (Ohi *et al.*, 2008). As already mentioned in §1, there are also indications for high-pressure polymorphs of orthoenstatite from experiment (Lin, 2003; Kung *et al.*, 2004). This transition occurs at about 10 GPa at room temperature. Recently, we could indeed identify two possible high-$P$ polymorphs, one with space group $P2_1ca$ and the other with space group *Pbca* (which will be

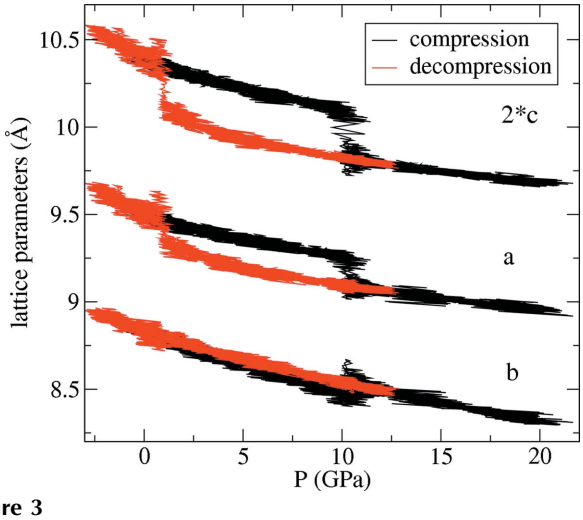


**Figure 3**
Evolution of the lattice parameters $a$, $b$ and $c$ across the low- to high-$P$ clinoenstatite transition from MD simulations at 300 K.

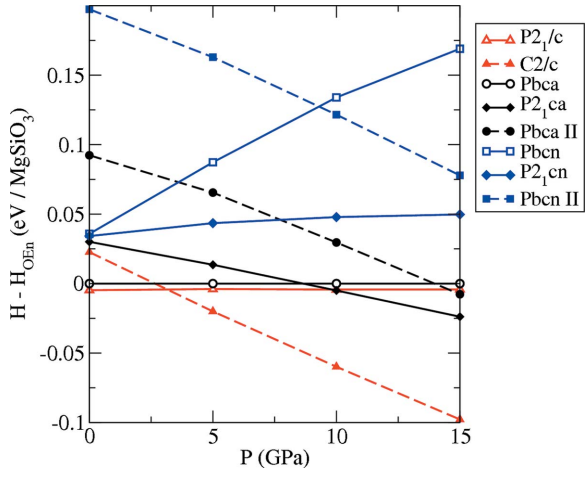


**Figure 4**
Enthalpy differences between various enstatite polymorphs and orthoenstatite ($H_{OEn}$) as a function of pressure from DFT calculations using the LDA. Red lines refer to clinoenstatites, black lines to orthoenstatites and blue lines to protoenstatites. The invidual structures are explained in the text.

denoted by *Pbca*-II in the following) (Jahn, 2008). The former seems to match better the X-ray diffraction data (Kung *et al.*, 2004). Furthermore, the DFT calculations predict this phase to become more stable than *Pbca* at about 9 GPa (see Fig. 4). The *Pbca*-II phase, which has the smallest volume of the orthoenstatite-related phases (Fig. 5), would become the most stable phase of this structure type above 20 GPa. The chain rotations change from pure O rotations in *Pbca* to 50% S rotation in *Pbca*-II with 25% S rotations for the intermediate $P2_1ca$ structure. The chains in the high-$T$ phase are again essentially extended.

Transitions in protopyroxenes are studied and observed less frequently. In $MgSiO_3$ the thermodynamic stability field is restricted to rather high temperatures and low pressures, which decreases the probability of observing metastable high-

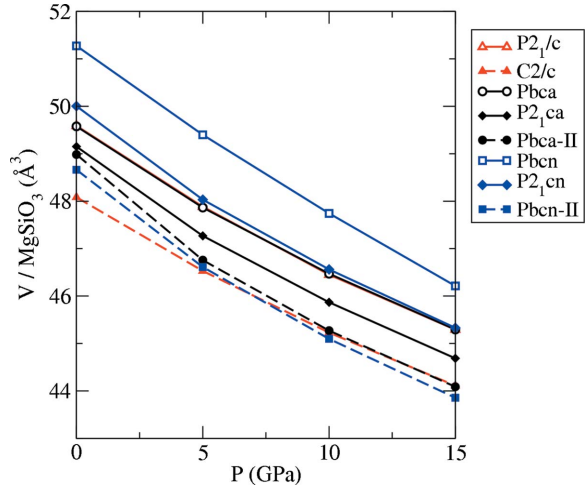


**Figure 5**
Volume per formula unit of various enstatite polymorphs as a function of pressure. Color codes and symbols correspond to those in Fig. 4. The volumes of orthoenstatite (*Pbca*) and low-clinoenstatite ($P2_1/c$) are virtually identical over the pressure range considered here.

*P* polymorphs experimentally. The transition from *Pbcn* protoenstatite to a high-pressure phase with $P2_1cn$ symmetry was observed for a slightly different chemical composition between 2.0 and 2.5 GPa (Yang *et al.*, 1999). From our MD simulations, we predict a second high-pressure phase, again with space group *Pbcn* (which we will refer to as *Pbcn*-II) (Jahn & Martoňák, 2009). The DFT calculations show a cross-over of the enthalpy curves between *Pbcn* and $P2_1cn$ at pressures close to 0 GPa (Fig. 4), which may shift to higher pressures at higher temperature. The high-density *Pbcn*-II phase has the lowest enthalpy in the protoenstatite system above 18 GPa. While *Pbcn* has only one type of almost extended O-rotated chains, half of the chains are S-rotated in $P2_1cn$. The *Pbcn*-II phase again consists of only one type, but in this case S-rotated chains (Jahn & Martoňák, 2009).

Owing to the relatively small energetic differences between some of the phases, we do not observe the intermediate high-pressure polymorphs of orthoenstatite ($P2_1ca$) and protoenstatite ($P2_1cn$) in the MD simulations. When either of these phases is used as a starting configuration, it is transformed to the lower-*P* or the higher-*P* phase (depending on the *P*–*T* conditions) after a very short duration MD simulation. This confirms the displacive character of the phase transitions described here with a rather low kinetic barrier, but also demonstrates the difficulty in describing the energetics accurately enough using our classical model. In Figs. 4 and 5 we summarize the results of the more accurate DFT calculations for the relative enthalpies and the volumes per formula unit as a function of pressure. We have included the major phases known from the phase diagram (except the high-*T* clinoenstatite) and our predicted high-pressure polymorphs of orthoenstatite (Jahn, 2008) and protoenstatite (Jahn & Martoňák, 2009). Structures with extended chains, which are represented here by *Pbcn* protoenstatite only, have the largest cell volumes and hence become very unfavorable towards high pressures. It is interesting to note that structures with almost parallel enthalpy slopes also have very similar volumes. Future studies may reveal the origin of the energetic differences between different $SiO_4$ chain stacking sequences.

### 3.2. Martensitic phase transitions

Structural transitions between the different structure types shown in Fig. 1 are of martensitic character and involve a rearrangement of the stacking order of $SiO_4$ chains. Stacking faults in pyroxenes have been investigated intensively by transmission electron microscopy (TEM) (Coe & Müller, 1973; Coe & Kirby, 1975; McLaren & Etheridge, 1976; Hugh-Jones *et al.*, 1996). From those studies it was concluded that the transition from orthoenstatite to low-clinoenstatite happens *via* slip parallel to the close-packed oxygen layers in the (100) plane along the chain direction, *i.e.* in the [001] direction. Furthermore, the transition is facilitated by the presence of an external non-hydrostatic stress field (Coe & Kirby, 1975). Another TEM study of dislocation glide in orthoenstatite (van Duysen *et al.*, 1985) suggests that, in addition to (100)[001], the (100)[010] slip system may also be activated. Experiments on the protoenstatite to ortho-/low-clinoenstatite transition using neutron scattering (Schrader *et al.*, 1990; Boysen *et al.*, 1991) show reversals that depend on the cooling rate.

Transitions to high-*P* clinoenstatite are much more difficult to access experimentally since high-*P* clinoenstatite transforms into low-clinoenstatite under decompression (see above). Computer simulations may provide insight into the nature of those transitions and constitute an *in situ* probe to study the actual process of the transitions, which allows the interpretation of the TEM snapshots to be checked. However, MD simulations alone are not able to overcome the large kinetic barriers of the transition. Metadynamics is the method of choice for searching for transition paths in this case. It should be noted that we do not model actual dislocations but rather look at collective shear between infinite crystals. Modeling of plastic deformations *via* dislocation glide is currently out of reach for direct atomistic simulation and alternative approaches have to be used (Carrez *et al.*, 2007).

In a number of metadynamics simulations coupled with classical MD, transitions between clino-, ortho- and protoenstatite phases were observed (Jahn & Martoňák, 2008, 2009). In Fig. 6 the evolution of the system enthalpy is shown for 600 metadynamics steps starting from low-clinoenstatite and running the simulation at ambient pressure and a temperature of 1500 K. The enthalpy shown represents the free energy of the system after removing non-hydrostatic stress from the simulation cell and after removing most of the kinetic energy in short MD simulations at constant pressure and (low) temperature. The lowest energy structures can be identified as either low-clinoenstatite or orthoenstatite. Intermediate high-energy structures are defect structures that may contain stacking faults and/or point defects. During the first transition from low-clinoenstatite to orthoenstatite that happens at metadynamics steps around 100, a high-energy

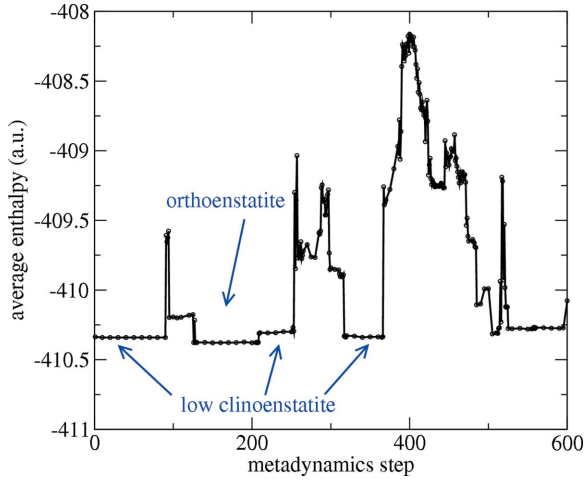


**Figure 6**
Enthalpy of relaxed configurations during combined metadynamics/MD simulation. The initial structure is low-clinoenstatite and simulations are performed at ambient pressure and 1500 K. While during the first transformation from low-clinoenstatite to orthoenstatite a number of intermediate high-energy structures are observed, the reverse transition essentially happens instantaneously.

barrier has to be crossed, while the reverse transition to low-clinoenstatite at metadynamics step 209 seems to be without intermediate steps. Similar behavior has also been observed in transitions at high pressure (Jahn & Martoňák, 2008, 2009).

Closer inspection suggests that the mechanisms found in the simulation seem to confirm the two suggestions made by experimentalists. It seems that at low temperatures and/or high pressures the shear mechanism that contains components in (100)[001] and (100)[010] is favored whereas the pure shear in (100)[001] becomes more important towards high temperatures and/or low pressures. Both mechanisms occurred during the metadynamics simulation of the protoenstatite to high-*P* clinoenstatite. They are illustrated in Figs. 7 and 8 viewed along the generalized *a* direction. The shear in Fig. 7 is dissociated into four partials and clearly has a strong shear component in the [010] direction, *i.e.* perpendicular to the chains. The three intermediate structures have a rather high energy. In the case of orthoenstatite the displacement vectors of the intermediate structures obtained from our simulations confirm the experimental observations (van Duysen *et al.*, 1985) and provide the components of the displacement vectors that were not accessible in the TEM studies (Jahn & Martoňák, 2008). In contrast, the second mechanism (Fig. 8) that involves only slip in (100)[001] happens without intermediate phases. While the first set of transitions involves some disorder on the Mg sites, there is a clear mechanism for the displacement of the Mg cations perpendicular to the chains, as indicated in Fig. 8. It appears that in the latter case Mg from *M*1 sites move to *M*2 sites and *vice versa*. For future projects it will be interesting to choose a system that has two different cations on the *M* sites and study their effect on the transition mechanisms.

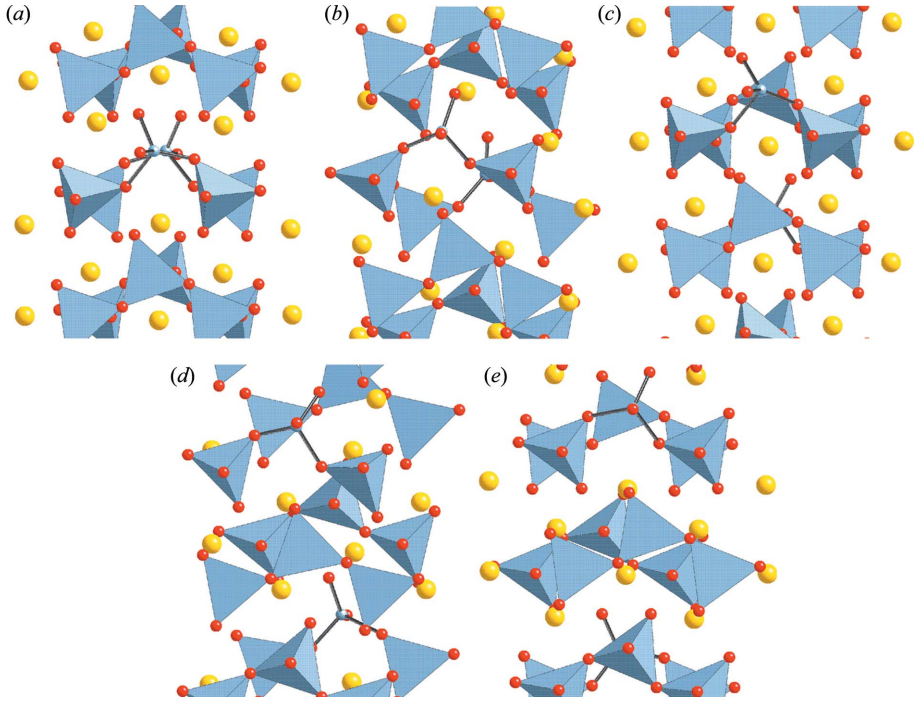


**Figure 7**
Reordering the stacking sequence of $SiO_4$ chains *via* dissociated mechanism. All structures are obtained after removing elastic strain from the simulation cell by MD. However, the intermediate structures have a rather high energy. The mechanism involves Si migration perpendicular to the chain direction.

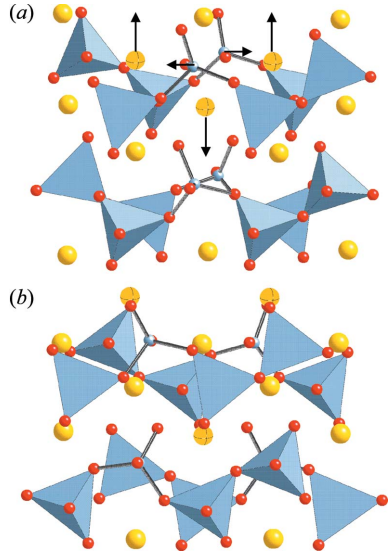


**Figure 8**
Illustration of the single-step mechanism for changing the stacking order of the chains before (*a*) and after (*b*) shear. The view is along the *a* axis and contains two layers of $SiO_4$ tetrahedra. Each layer is represented by two chains, one with apices pointing upwards and the other downwards. Silicon atoms are essentially displaced only along the chain direction and Mg atoms perpendicular to it. The shear is accompanied by rotations within the chains. Four of the $SiO_4$ tetrahedra are drawn as balls and sticks and three of the Mg (large yellow balls) are marked with equatorial lines. O atoms are represented by small red balls.

## 4. Conclusions

The case study of $MgSiO_3$ pyroxenes demonstrates impressively the strength of computer simulations for studying phase behavior in complex materials. The combination of various techniques ranging from quantum-mechanical approaches *via* classical interaction potentials to methods such as metadynamics is especially useful for exploring the free energy landscape very accurately in a rather narrow range of configurations. Even for a relatively well studied system such as enstatite, interesting new phases are predicted and may be observed in the future. Furthermore, an integrated computational study as presented here has linked very nicely experi-

mental work of 30 years. In this respect, complementary experimental and simulation studies seem to have great potential not only but certainly in geomaterials science.

I would like to thank R. Martoňák for providing the metadynamics code. Part of this work was supported by DFG grant JA 1469/4-1.

## References

Aguado, A., Bernasconi, L., Jahn, S. & Madden, P. A. (2003). *Faraday Discuss.* **124**, 171–184.
Allen, M. P. & Tildesley, D. J. (1987). *Computer Simulations of Liquids.* Oxford University Press.
Angel, R. J., Chopelas, A. & Ross, N. L. (1992). *Nature (London)*, **358**, 322–324.
Boysen, H., Frey, F., Schrader, H. & Eckold, G. (1991). *Phys. Chem. Miner.* **17**, 629–635.
Carrez, P., Ferre, D. & Cordier, P. (2007). *Nature (London)*, **446**, 68–70.
Coe, R. S. & Kirby, S. H. (1975). *Contrib. Mineral. Petrol.* **52**, 29–55.
Coe, R. S. & Müller, W. F. (1973). *Science*, **180**, 64–66.
Duysen, J. C. van, Doukhan, N. & Doukhan, J. C. (1985). *Phys. Chem. Miner.* **12**, 39–44.
Gonze, X. *et al.* (2002). *Comput. Mater. Sci.* **25**, 478–492.
Gonze, X. *et al.* (2005). *Z. Kristallogr.* **220**, 558–562.
Green, H. W. II (2007). *Proc. Natl Acad. Sci. USA*, **104**, 9133–9138.
Hugh-Jones, D., Sharp, T., Angel, R. & Woodland, A. (1996). *Eur. J. Mineral.* **8**, 1337–1345.
Jackson, J. M., Sinogeikin, S. V., Carpenter, M. A. & Bass, J. D. (2004). *Am. Mineral.* **89**, 239–245.
Jahn, S. (2008). *Am. Mineral.* **93**, 528–532.
Jahn, S. & Madden, P. A. (2007). *Phys. Earth Planet. Inter.* **162**, 129–139.
Jahn, S. & Martoňák, R. (2008). *Phys. Chem. Miner.* **35**, 17–23.
Jahn, S. & Martoňák, R. (2009). *Am. Mineral.* **94**, 950–956.
Kung, J., Li, B., Uchida, T., Wang, Y., Neuville, D. & Liebermann, R. C. (2004). *Phys. Earth Planet. Inter.* **147**, 27–44.
Lin, C.-C. (2003). *J. Solid State Chem.* **174**, 403–411.
McLaren, A. C. & Etheridge, M. A. (1976). *Contrib. Mineral. Petrol.* **57**, 163–177.
Madden, P. A., Heaton, R., Aguado, A. & Jahn, S. (2006). *J. Mol. Struct. (Theochem)*, **771**, 9–18.
Martoňák, R., Donadio, D., Oganov, A. & Parrinello, M. (2006). *Nat. Mater.* **5**, 623–626.
Martoňák, R., Laio, A., Bernasconi, M., Ceriani, C., Raiteri, P., Zipoli, F. & Parrinello, M. (2005). *Z. Kristallogr.* **220**, 489–498.
Martoňák, R., Laio, A. & Parrinello, M. (2003). *Phys. Rev. Lett.* **90**, 075503.
Martyna, G. J., Tobias, D. J. & Klein, M. L. (1994). *J. Chem. Phys.* **101**, 4177–4189.
Mendelssohn, M. J. & Price, G. D. (1997). *Phys. Chem. Miner.* **25**, 55–62.
Miyake, A., Shimobayashi, N., Miura, E. & Kitamura, M. (2002). *Phys. Earth Planet. Inter.* **129**, 1–11.
Monkhorst, H. J. & Pack, J. D. (1976). *Phys. Rev. B*, **13**, 5188–5192.
Nosé, S. & Klein, M. L. (1983). *Mol. Phys.* **50**, 1055–1076.
Oganov, A. R. & Glass, C. W. (2006). *J. Chem. Phys.* **124**, 244704.
Ohi, S., Miyake, A., Shimobayashi, N., Yashima, M. & Kitamura, M. (2008). *Am. Mineral.* **93**, 1682–1685.
Perdew, J. P. & Zunger, A. (1981). *Phys. Rev. B*, **23**, 5048–5079.
Perrotta, A. J. & Stephenson, D. A. (1965). *Science*, **148**, 1090–1091.
Presnall, D. C. (1995). *Mineral Physics and Crystallography, A Handbook of Physical Constants*, Vol. 2 of *AGU Reference Shelf*, pp. 248–268. Washington: American Geophysical Union.
Rappe, A. M., Rabe, K. M., Kaxiras, E. & Joannopoulos, J. D. (1990). *Phys. Rev. B*, **41**, 1227–1230.
Schön, J. C. & Jansen, M. (1996). *Angew. Chem. Int. Ed.* **35**, 1286–1304.
Schrader, H., Boysen, H., Frey, F. & Convert, P. (1990). *Phys. Chem. Miner.* **17**, 409–415.
Shimobayashi, N., Miyake, A., Kitamura, M. & Miura, E. (2001). *Phys. Chem. Miner.* **28**, 591–599.
Smith, J. V. (1969). *Nature (London)*, **222**, 256–257.
Stone, A. J. (1996). *The Theory of Intermolecular Forces.* Oxford University Press.
Tang, K. T. & Toennies, J. P. (1984). *J. Chem. Phys.* **80**, 3726–3741.
Thompson, R. M. & Downs, R. T. (2003). *Am. Mineral.* **88**, 653–666.
Wilson, M., Madden, P. A. & Costa-Cabral, B. J. (1996). *J. Phys. Chem.* **100**, 1227–1237.
Yang, H., Finger, L. W., Conrad, P. G., Prewitt, C. T. & Hazen, R. M. (1999). *Am. Mineral.* **84**, 245–256.